Two-dimensional graded metamaterials with auxetic rectangular perforations

Jianfei Yao[a,b,c,1], Rujie Sun[d,1], Fabrizio Scarpa[e,f], Chrystel Remillat[e], Yu Gao[a,b], Yongfei Su[a,b]

[a] College of Mechanical and Electrical Engineering, Beijing University of Chemical Technology, Beijing, 100029, China

[b] Beijing Key Laboratory of Health Monitoring and Self-recoverying for High-end Mechanical Equipment, Beijing University of Chemical Technology, Beijing, 100029, China

[c] Key Lab of Engine Health Monitoring-Control and Networking of Ministry of Education, Beijing University of Chemical Technology, Beijing, 100029, China

[d] Department of Materials, Department of Bioengineering and Institute of Biomedical Engineering, Imperial College London, Prince Consort Road, London SW7 2AZ, UK

[e] Bristol Composites Institute (ACCIS), University of Bristol, Bristol BS8 1TR, UK

[f] Dynamics and Control Research Group (DCRG), University of Bristol, Bristol BS8 1TR, UK

(Corresponding author: Fabrizio Scarpa, Email: f.scarpa@bristol.ac.uk; Jianfei Yao, Email: yaojf@mail.buct.edu.cn

[1] These authors contributed equally to this work.)

This work describes the in-plane uniaxial tensile mechanical properties of two-dimensional graded rectangular perforations metamaterials using numerical homogenization finite element approaches benchmarked by experimental results. The metamaterial configuration is based on graded patterns of centre-symmetric perforated cells that can exhibit an auxetic (negative Poisson's ratio) behavior. Global and local equivalent mechanical properties of the metamaterial are measured using digital image correlation techniques mapped over Finite Element models to identify strain patterns and related stress distributions at different scales. The samples and their numerical counterpart are parametrized against the spacing and aspect ratios of the cells. The overall stiffness behavior of the graded perforated metamaterial plates features a higher degree of compliance that depends both on the geometries of the cells of the graded areas, but also on the graded pattern used. Local Poisson's ratio effects show a general constraint of the auxetic behavior compared to the case of uniform plates, but also interesting and controllable shape changes due to the uniaxial tensile loading applied.

Key words: Mechanical metamaterials, composites, rectangular perforations, gradient structures, negative Poisson's ratio

1 Introduction.

Functionally gradient and graded materials have been extensively developed during the last decades to generate multifunctionalities and unusual mechanical properties by geometry and material tailoring [1, 2]. As a subset of functional graded solids and mechanical metamaterials, the concept of cellular gradient configurations has been also explored by few Authors in relatively recent times. Lim was probably the first to identify a continuous gradient topology of center-symmetric cells showing a Poisson's ratio curving effect [3]. Thickness-gradient honeycombs have been evaluated experimentally and numerically by Lira and Scarpa [4], and gradient cellular topologies have been exploited for possible vibroacoustics and modal tuning of high-end structures [5-8]. Sandwich structures with periodic alternated graded cellular cores have been designed and modelled for tailored bandgap behavior [9] and manufactured using Kirigami techniques [10]. All those mechanical metamaterial configurations have one or the whole topology showing auxetic (negative Poisson's ratio) deformation mechanisms, applied in particular to mitigate blast and improve the mechanical response of structure under dynamic loading. This has focused on re-entrant [11, 12] and planar oval configurations [13] under static and dynamic loading [14]. Gradient cellular cores have been also evaluated from a structural integrity and energy absorption point of view in sandwich beams subjected to 3-point bending [15] and for crashworthiness applications in 2D and 3D lattices and porous materials and related structures [16-19]. In terms of wave propagation, Trainiti et al have shown that graded undulated configurations are able to provide localization and wave trapping phenomena [20]. Graded designs of auxetic [21, 22] and conventional Poisson's ratio units have been used to develop programmable metamaterials with pre-defined deformation patterns [23]. In general, these gradient cellular and semi-periodic configurations provide an excellent platform for topological and machine learning-driven design of mechanical metamaterials [24, 25].

The mechanical metamaterial concept described in this work is based on the use of patterned perforations that provide an auxetic (negative Poisson's ratio - NPR) deformation mechanism [26]. Perforations or porous patterns exhibiting NPR have been identified by Sigmund by using topological optimization [27], and then further developed by Grima et al with rectangular and rhomboidal configurations [28, 29]. Perforations have been used to generate global auxetic

behaviors in plates or 2D substrates [13, 30, 31], or to create hierarchical configurations with tailored properties [32-35]. The specific perforation topology used in this work is the one presented in Slann et al [36]. The center-symmetric perforated configuration is particularly apt for a graded/gradient topology, because of the ease of adjusting the geometry parameters that define the porous areas to build geometrically consistent gradient patterns. Another advantage of this configuration in terms of manufacturing is the fact that by reducing the perforation aspect ratio (see more details later), it is possible to better approximate the narrow cuts/slits sheet configurations developed in [31, 33] and using therefore a broader set of manufacturing tools, from laser cutters to mechanical cutters/punchers on a wide set of substrates (metal, thermosets, thermoplastics, paper). This facilitates the use of gradient cellular/perforated plates in a variety of applications and materials at relatively low cost.

2 Methodology

2.1 Unit cell with the rectangular perforations

The geometry parameters that characterize the unit cell are shown in Fig.1 [36]. The width of the void area has length a and b is the maximum vertical height of the perforation. The length of the unit cell is L and s defines the horizontal distance between two vertices of the voids. The center symmetry of the cell allows to define the whole topology of the unit using two parameters: the void aspect ratio (AR) and the intercell spacing (IS). The AR and the IS parameters can be directly calculated as:

$$AR=a/b \quad (1)$$

$$IS=s/L \quad (2)$$

The gradient topology was created by varying the nondimensional parameters and the length of the cell through two limits: AR=5 and L=18mm, and AR=4 and L=20mm. Changes of the IS parameter were made from 0.1 to 0.3. Table 1 shows how the aspect ratios and the intercell spacing change in the gradient/graded topology that will be described later.

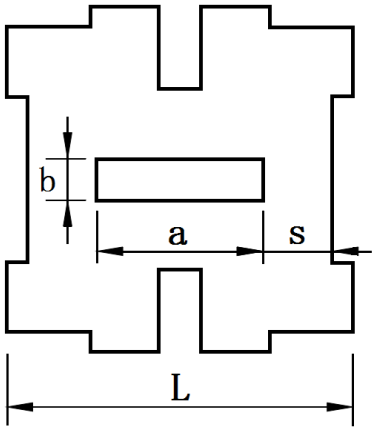

Fig.1 Perforation unit cell

Table 1 Changes in AR and IS parameters for the unit cells with the rectangular geometry

		IS				
		0.1	0.15	0.2	0.25	0.3
L	18mm					
AR	5					
L	20mm	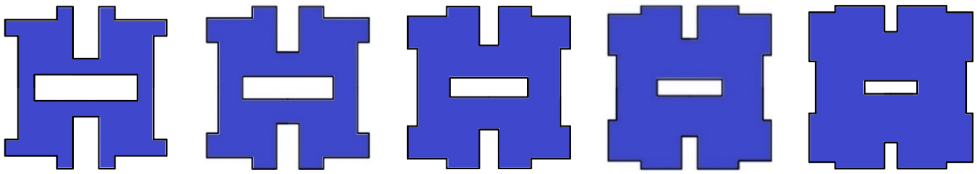				
AR	4					

2.2 Two-dimensional gradient cellular plates with rectangular geometry shape perforations

The configuration in this gradient topology is made of a continuous distribution of unit cells with compatible geometry but having variable parameters (like the void aspect ratio or intercell spacing). We consider here three designs (Figure 2): a linear gradient (type A) and two graded configurations (types B and C). The linear gradient structure involves a series of unit cells with IS values gradually changing from the largest one (0.3) on the top side of the sheet to the

smallest (0.1) on the opposite end. The graded configuration B has unit cells with IS values gradually changing from 0.1 in the middle to 0.3 at the two opposite edges of the sheet. Type C configuration has instead IS cell values gradually changing from the smallest one (0.1) at the two ends of the plate to the largest one at the middle region.

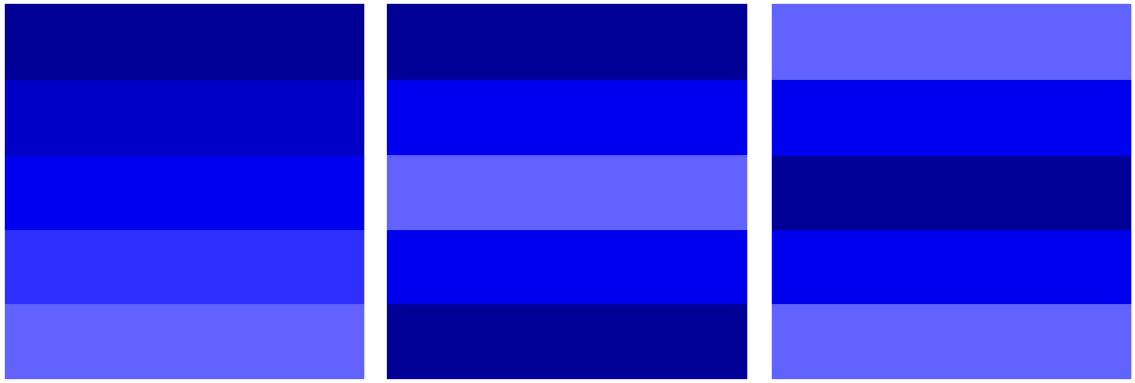

(a) Type A (b) Type B (c) Type C

Fig.2 The gradient/graded distributions involving five types of unit cells (the darkest colour indicates regions in which the value of the cell IS is the largest; lighter blue indicates an area with cell having the smallest IS)

3 Manufacturing and experimental tests

The specimens have been produced by using a laser cutting facility (World Lasers LR1612 laser cutter with a 40W CO2 laser) to pattern PMMA substrates. The elastic mechanical properties of the PMMA material have been determined following the ASTM D638-08 standard. The tests have been performed using a Shimadzu Machine (10KN load cell, 1mm/min) with dog-bone specimens (Type V, T=3mm). The PMMA specimens have a Young's modulus of 2.90±0.43 GPa and a Poisson's ratio of 0.37±0.03, the latter determined using a video gauge extensometer. These properties are used to develop the FE models. A CAD model of the cellular plates has then been exported to the laser cutting machine to generate the rectangular perforations configurations. Six gradient samples have been produced. The samples have been denominated with a G code indicating gradient, and a U code standing for uniform. Specimens with L=18mm, AR=5 (geometry 1, G1) for type A, type B and type C, and L=20mm, AR=4 (geometry 2, G2) for type A, type B and type C have been produced. All samples consisted in assemblies of 8 X 10 cells. The dimensions of the samples subjected to uniaxial tensile test are 280mm X 144mm X 3mm for the specimens related to geometry #1, and 300mm X 160mm X 3mm for specimens

related to geometry #2. The six samples are been therefore named as G1-A, G1-B, G1-C, G2-A, G2-B, and G2-C. The parameters of the gradient samples are shown in Table 2. For comparison, six uniform (i.e., constant unit cell) samples were fabricated, and the parameters of the uniform samples are also shown in Table 3.

Table 2 Parameters of the gradient samples

No.	**Type**	**AR**	**Dimensions**
Sample G1-A	A	5	280mm X 144mm X 3mm
Sample G1-B	B	5	280mm X 144mm X 3mm
Sample G1-C	C	5	280mm X 144mm X 3mm
Sample G2-A	A	4	300mm X 160mm X 3mm
Sample G2-B	B	4	300mm X 160mm X 3mm
Sample G2-C	C	4	300mm X 160mm X 3mm

Table 3 Parameters of the uniform samples

No.	**IS**	**AR**	**Dimensions**
Sample G1-U-1	0.1	5	280mm X 144mm X 3mm
Sample G1-U-2	0.2	5	280mm X 144mm X 3mm
Sample G1-U-3	0.3	5	280mm X 144mm X 3mm
Sample G2-U-1	0.1	4	300mm X 160mm X 3mm
Sample G2-U-2	0.2	4	300mm X 160mm X 3mm
Sample G2-U-3	0.3	4	300mm X 160mm X 3mm

Table 4 the IS values of the regions for the types

Regions	Type A	Type B	Type C
1	0.3	0.3	0.1
2	0.25	0.2	0.2
3	0.2	0.1	0.3
4	0.15	0.2	0.2
5	0.1	0.3	0.1

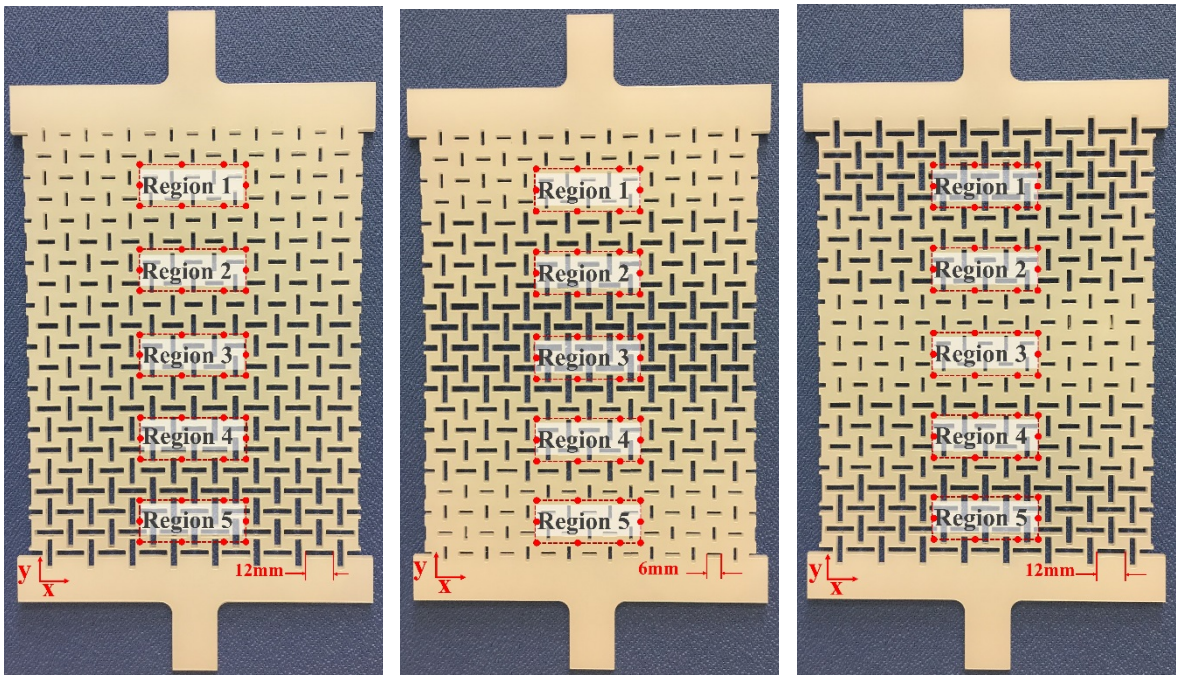

(a) Type A (b) Type B (c) Type C

Fig.3 Gradient samples fabricated by laser cutting

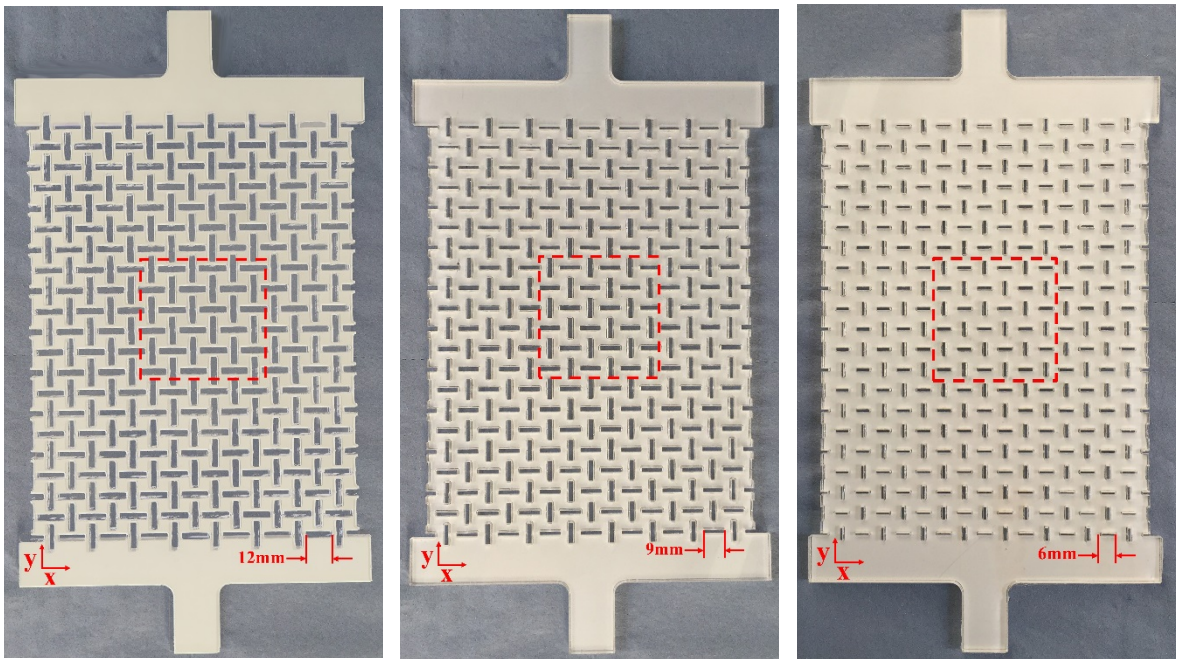

(a) IS=0.1 (b) IS=0.2 (c) IS=0.3

Fig.4 Uniform (constant cell) samples

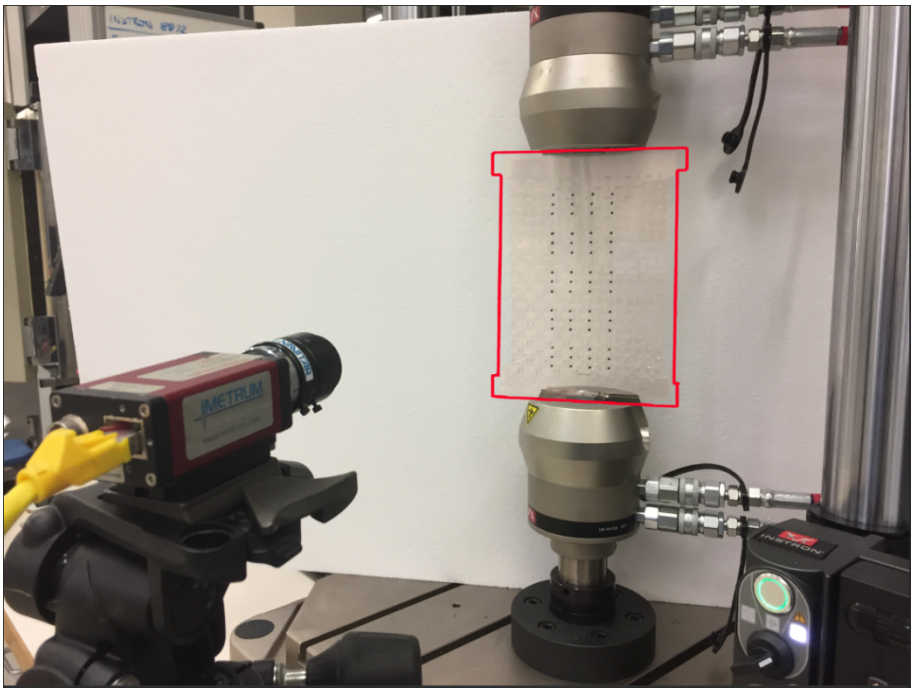

Fig.5 Uniaxial tensile rig setup and DIC instrumentation

Displacement were evaluated by post processing the DIC (Digital Image Correlation) images, during which correlations have been performed between pixels within successive images. The DIC kit consisted in a iMetrum camera and a Video Gauge™ software. Strains were then calculated through displacement coordinates at the four corners of the central area of interest, with a reference distance from the first frame used for baseline. The stress was obtained by dividing the load by the equivalent cross-sectional area of the specific region. The equivalent cross-sectional area of one region can be calculated as:

$$S = \sum_{i=1}^{n} \frac{b_i}{H} \left(L - \sum_{j=1}^{k} a_{ij} \right) d \tag{3}$$

Where S is the equivalent cross-sectional area of the region, b_i is the vertical height of the perforation for the i^{th} region and a_i is the width of the void area for the same i^{th} section. The thickness of the sample is d, L is the width of the sample and H is the height of one region in the gradient sample.

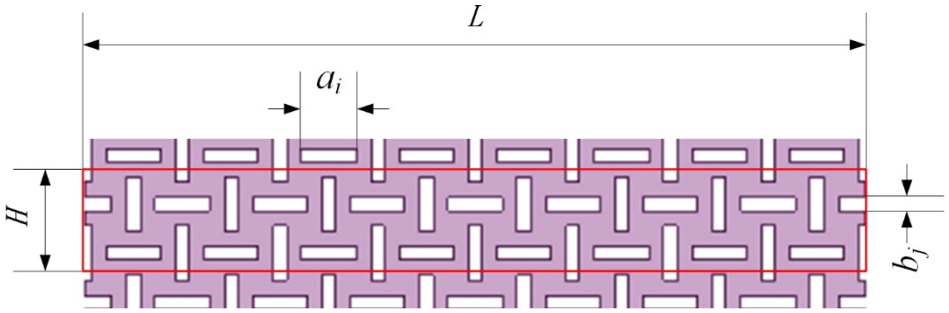

Fig 6 Schematics of the parameters of the equivalent cross-sectional area for one specific region

The Young's modulus and Poisson's ratio were then calculated with the classical formula:

$$E=\sigma_y/\varepsilon_y \quad (4)$$

$$\nu= -\varepsilon_x/\varepsilon_y \quad (5)$$

Where ε_x is the average lateral strains, ε_y is the average longitudinal strains, and σ_y is the average stresses respectively.

The Young's modulus was calculated as the slope of the stress-strain curve up to 0.3% of tensile strain. The Poisson's ratios were also calculated considering tensile strains with the limit above.

4 Modeling

Finite element simulations were carried out using the commercial software ANSYS Workbench. 19.0 to simulate the in-plane linear elastic properties of the specimens. Three-dimensional models were built using the CAD software Creo Parametric 2.0. Within ANSYS, the SOLID186 (three-dimensional 20-node) element was selected. Each node of the element possesses three translational degrees of freedom (x, y and z directions). Key points on the models were marked in SpaceClaim and positioned to track the deformation changes in the area of interest. A MultiZone mapping meshing technique has been applied with mesh size adjusted appropriately before solving. The mesh element size was set at 1mm (mesh quality parameter of 100). The relevance center level is selected as "fine" to ensure that the narrow gaps existing within the structure can include more than one grid. A set fixed constraints and displacement constraints on the boundary of the holding position were placed to simulate the tensile test. During the post-processing, the results were acquired within the equivalent elastic strain of the whole PMMA material, and the displacements at nodes corresponding to the DIC measurement dots were measured. Figure 7 shows the numerical results related to the six experimental samples.

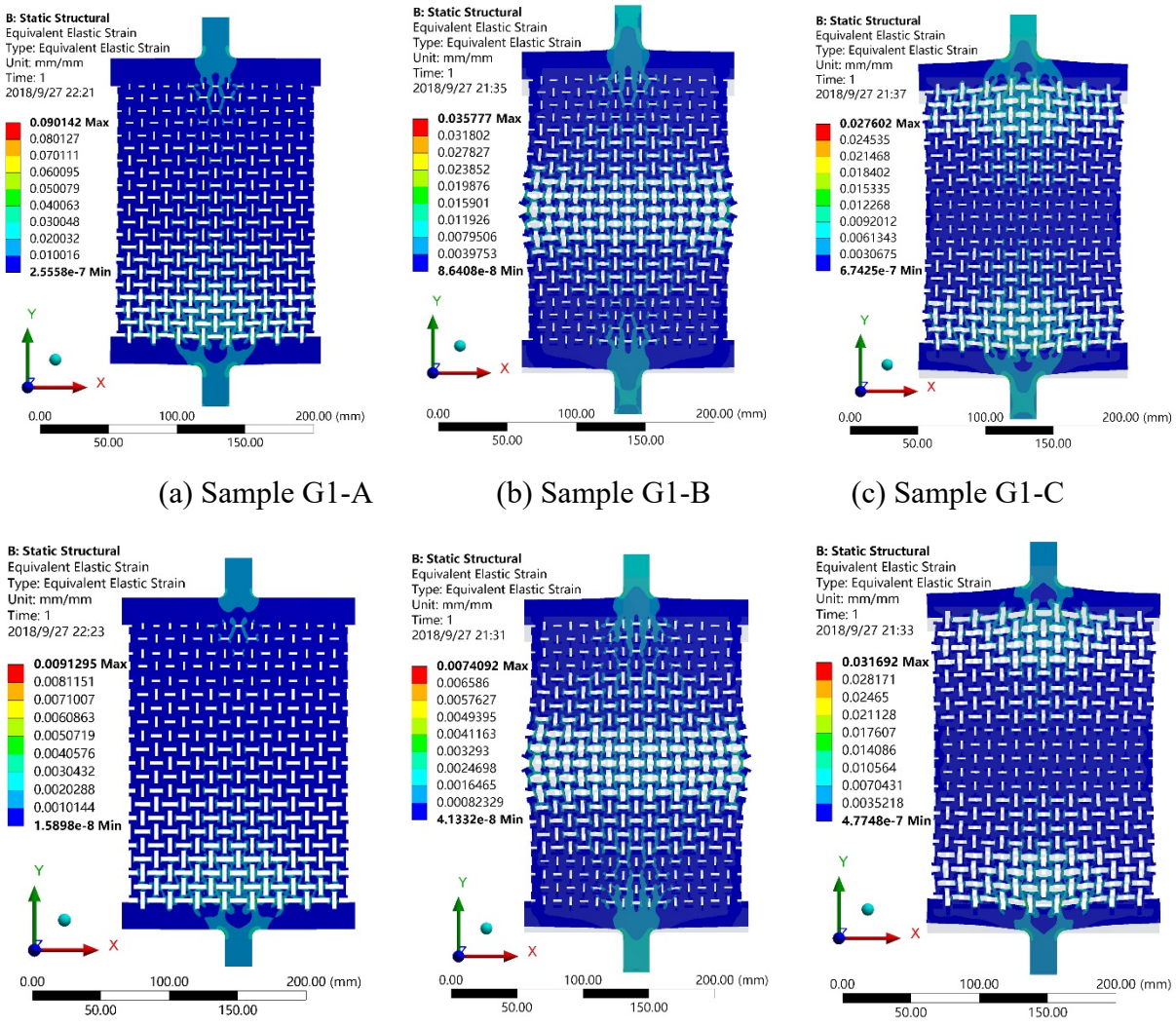

(a) Sample G1-A (b) Sample G1-B (c) Sample G1-C

(d) Sample G2-A (e) Sample G2-B (f) Sample G2-C

Fig.7 FE strain patterns for samples of type A, B and C

5 Results and discussion

5.1 Young's modulus and stiffness

It is possible to observe a very good agreement between the FE and the experimental results related to the uniform samples (Table 5), with discrepancies between ~ 5% and 12% maximum in terms of Young's modulus. Those results are also consistent with the findings from Slann et al [36] related to uniform perforated samples made of ABS plastics. Similarly to the results reported in the latter citation, the interspace ratio is the parameter that drives the higher stiffness for a given aspect ratio of the unit cell.

Figure 8 shows the stress-strain curves related to the G1 and G2 samples. The curves show a fairly marked linearity before brittle failure, the last caused by the mechanical behavior of the

PMMA polymer of the plates. The three G1 architectures show a quite similar behavior, with only failure strains and stresses at different levels. Similar considerations can also be made for the G2 configurations, although the G2-C shows a slightly lower global stiffness after a 0.15% tensile strain compared to the other two. This may be also explained by the large compliance at the end plates (see Fig. 7(f)) that could induce some lower load transfer to the rest of the stiffer gradient architecture when the tensile strain increases. The global Young's moduli predicted by the FE do not substantially differ between each other, all ranging between 0.356 GPa and 0.374 GPa (Fig.9). The experimental results tend in general to show a similar trend to the one featured by the numerical data, with maximum discrepancies of 12% (Fig. 9). The use of perforations provides a knock-down effect on the global stiffness of the pristine plates (~86% decrease of the Young's modulus compared to the one of PMMA samples). The global Young's modulus of the gradient configurations has a magnitude that is intermediate between the ones of the uniform cell distribution plates with the lowest and highest IS values (Table 5 and Fig.9). The moduli are always higher than the ones referring to the lowest IS configurations (~ 4 times higher), but significantly lower (~ 5 times) compared to the uniform configurations with the highest IS value in the gradient architecture.

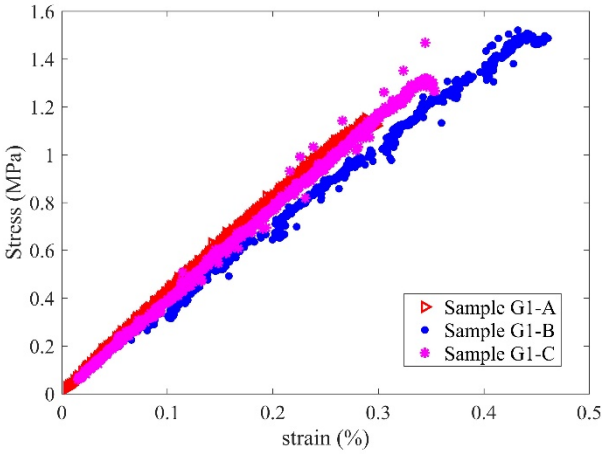

(a) Samples G1

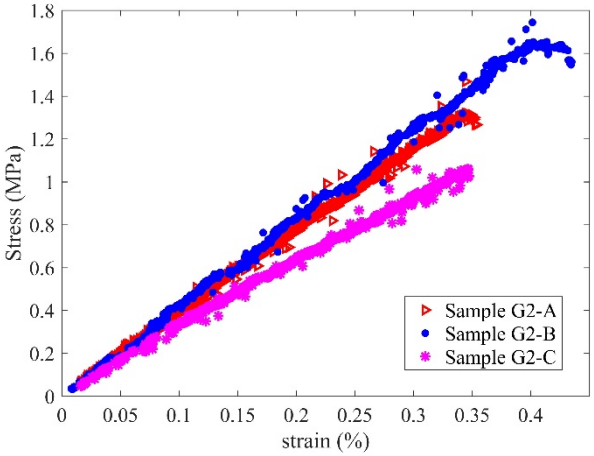

(b) Samples G2

Fig.8 Global tensile stress-strain curves for the two geometries (samples G1 and G2)

Table 5 Comparison between the experimental and numerical results of the Young's moduli for the uniform samples

NO.	FEM [GPa]	Experiment [GPa]
Sample G1-U-1	0.085	0.081±0.007
Sample G1-U-2	0.612	0.647±0.130
Sample G1-U-3	1.299	1.328±0.165
Sample G2-U-1	0.093	0.088±0.008
Sample G2-U-2	0.731	0.729±0.032
Sample G2-U-3	1.537	1.748±0.199

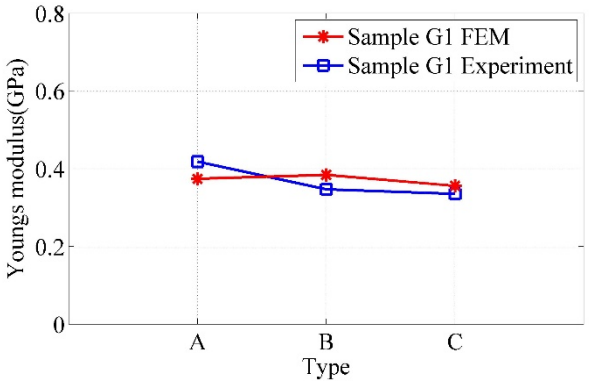

(a) Samples G1

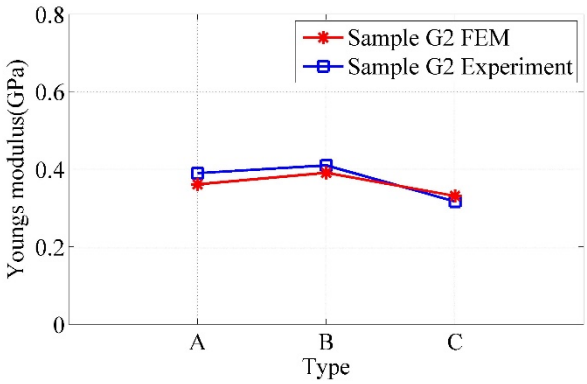

(b) Samples G2

Fig.9 Global Young's modulus of the gradient samples

At local level (i.e., area of the band grading) the stiffness has been evaluated as the ratio between the stress and the mapped strains of the selected region. The stiffness at area level was obtained by post-processing the experimental DIC strains (Fig. 10); the linear elastic stresses along the y-direction were mapped at FE level to reconstruct the local level. The stress-strain curves at local level (Fig. 10) show that regions with higher compliance provide larger strain to failures (between 8% and 10% in regions #1 for all the samples shown here). Those strains to tensile failure values are well beyond the usual 4%-6% range of pristine (unperforated) PMMA.

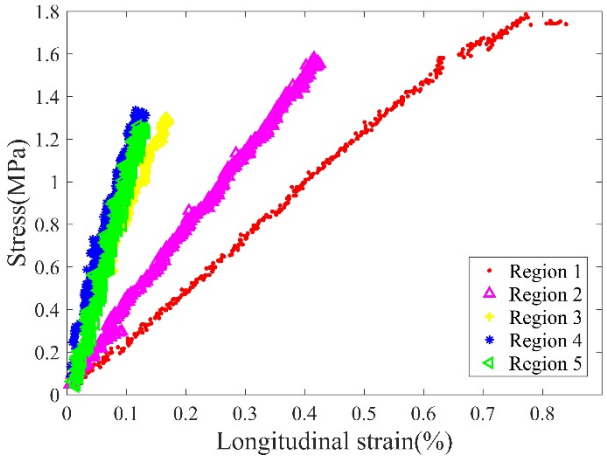

(a) Sample G1-A

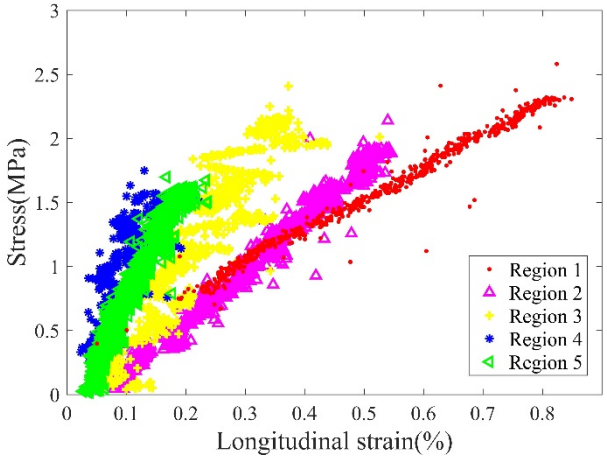

(b) Sample G2-A

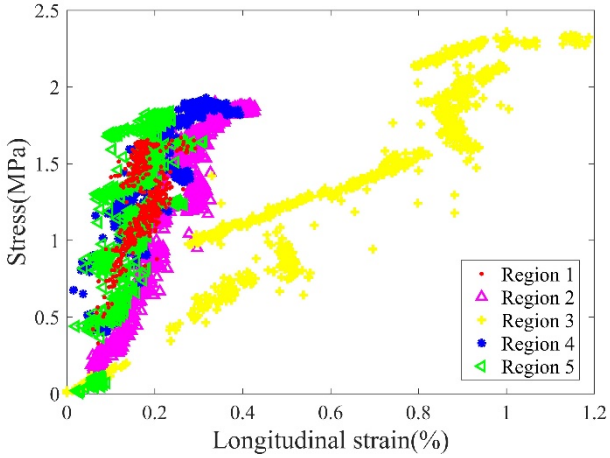

(c) Sample G1-B

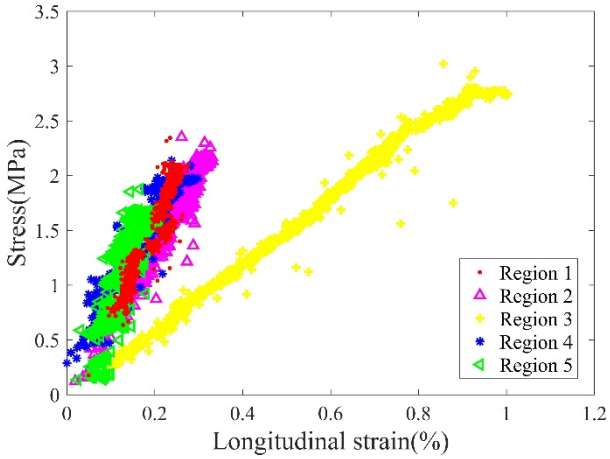

(d) Sample G2-B

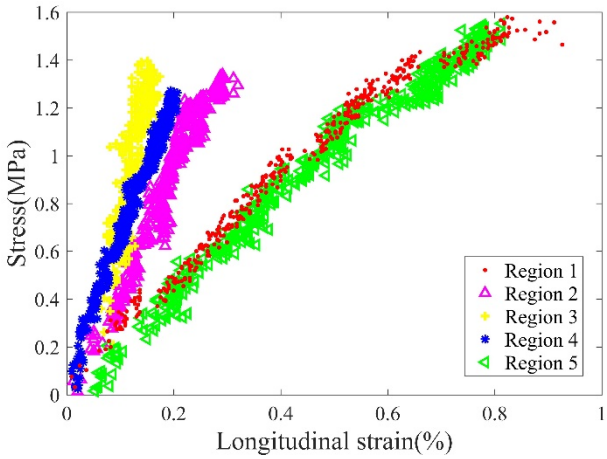

(e) Sample G1-C

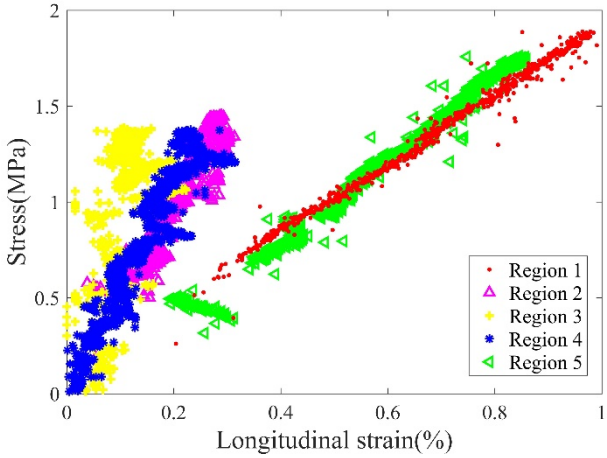

(f) Sample G2-C

Fig.10 Local tensile stress-longitudinal strain curves for the gradient samples of types A, B and C

The distribution of the local stiffness in the gradient samples shows a common trend between the FE and the experimental results (Fig. 11). Discrepancies however vary between 0.1% in the first region of sample G1-A to a maximum of 33% in region #3 for sample G1-C. The FE tends to follow the behavior of the experimental results, although it overestimates the stiffness in the G1-C and G2-C regions, especially the central ones.

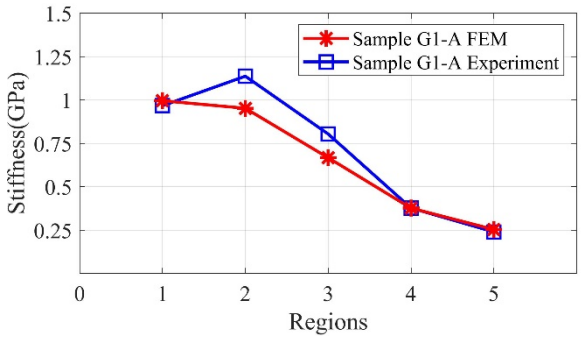

(a) Sample G1-A

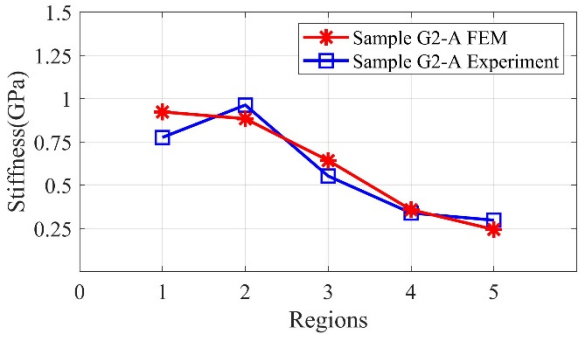

(b) Sample G2-A

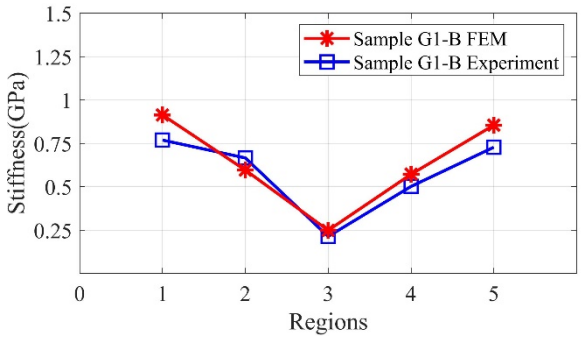

(c) Sample G1-B

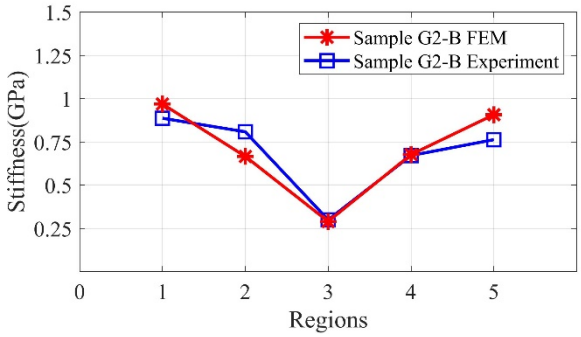

(d) Sample G2-B

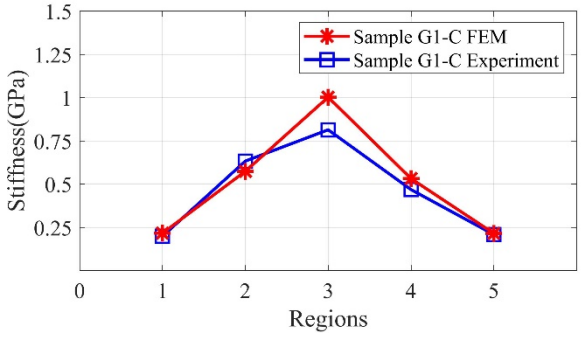

(e) Sample G1-C

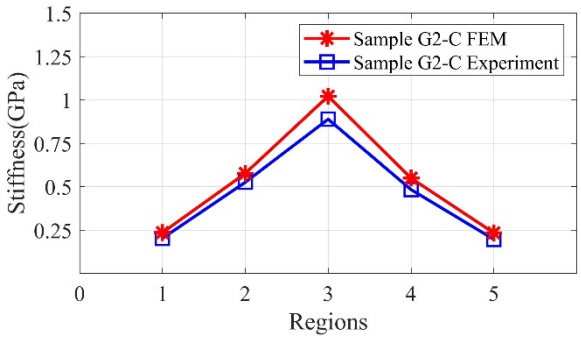

(f) Sample G2-C

Fig.11 Local stiffnesses in the gradient samples

5.2 Poisson's ratios

Table 6 shows a direct comparison between numerical and experimental Poisson's ratios measured in the uniform samples. Discrepancies between the two sets of results are up to ~6% in the case of sample G2-U-3, otherwise the other specimens show divergences from the experimental data of a maximum of 1%. All the architectures shown here are auxetic, apart from the ones of samples G1-U-3 and G2-U-3, all with interspace ratios of 0.3. Those values of IS do generate configurations with in-plane positive Poisson's ratio at aspect ratio values higher than 3 [36]. The Poisson's ratios show a substantial good linearity until ~ 0.4% of tensile strain (Fig. 12).

Table 6 Comparison between Experimental and numerical results for the Poisson's ratio in the uniform samples

NO.	FEM	experiment
Sample G1-U-1	-0.788	-0.796±0.02
Sample G1-U-2	-0.172	-0.179±0.05
Sample G1-U-3	0.395	0.393±0.04
Sample G2-U-1	-0.765	-0.772±0.02
Sample G2-U-2	-0.097	-0.095±0.04
Sample G2-U-3	0.438	0.465±0.05

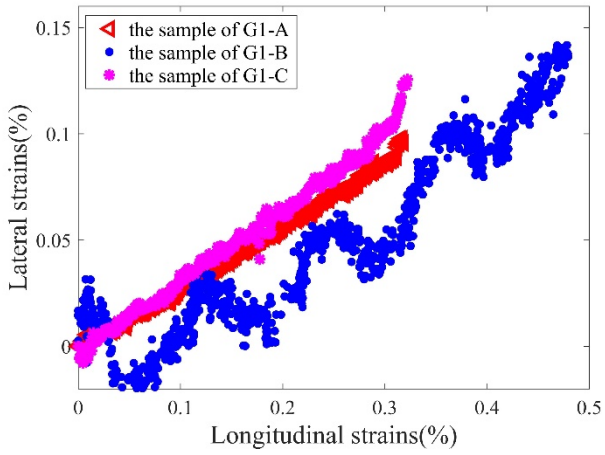

(a) Samples G1

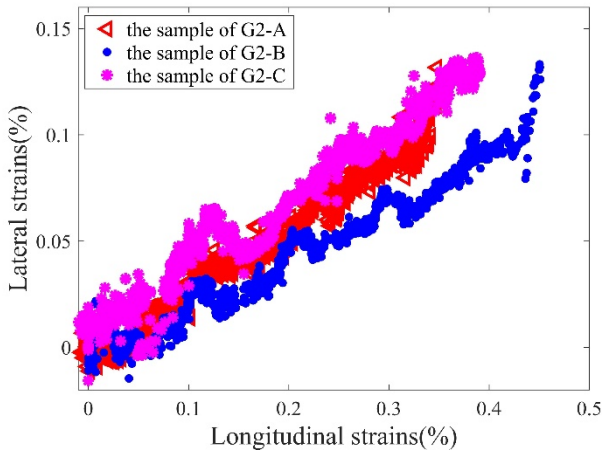

(b) Samples G2

Fig 12 Global lateral versus longitudinal strains for the gradient samples of types A, B and C

Local Poisson's ratio

All samples show a fairly good linearity between longitudinal (y) and lateral strain (x) about 0.05% and 0.8% of longitudinal strain (Figure 13). The highest level of linear correlation between strains is however recorded in samples G1-A, G2-B and G1-C. The lateral versus longitudinal strain curves have the largest slopes in regions when the cells have the smallest interspace distance. Regions at the edges of the metamaterial plates (1 and 5) tend to feature lower slopes compared to the other graded cellular areas.

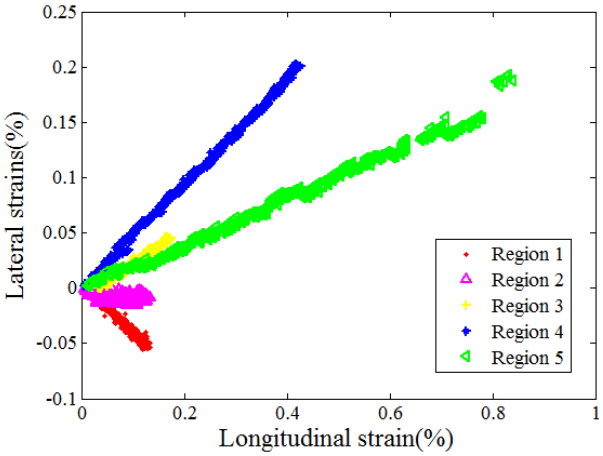

(a) Sample G1-A

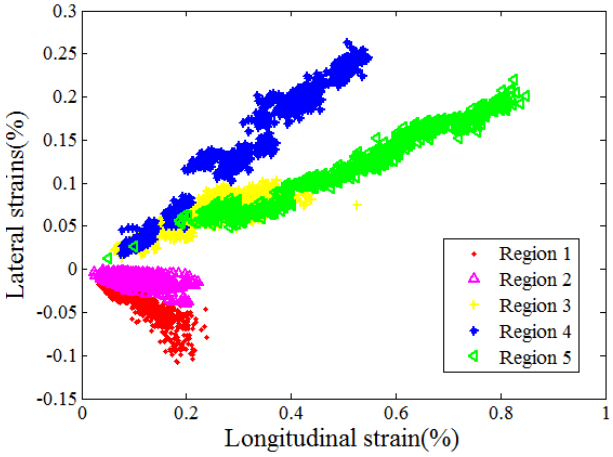

(b) Sample G2-A

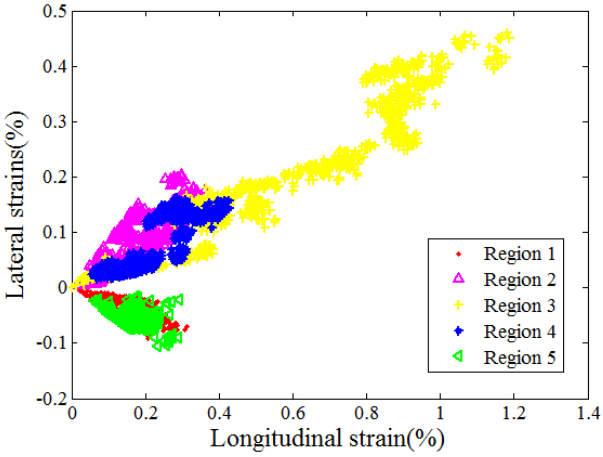

(c) Sample G1-B

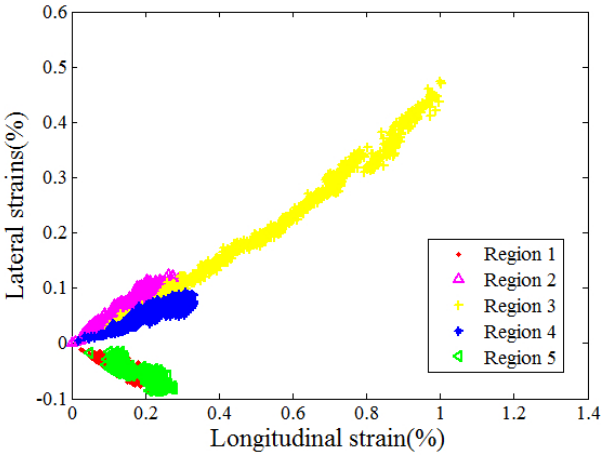

(d) Sample G2-B

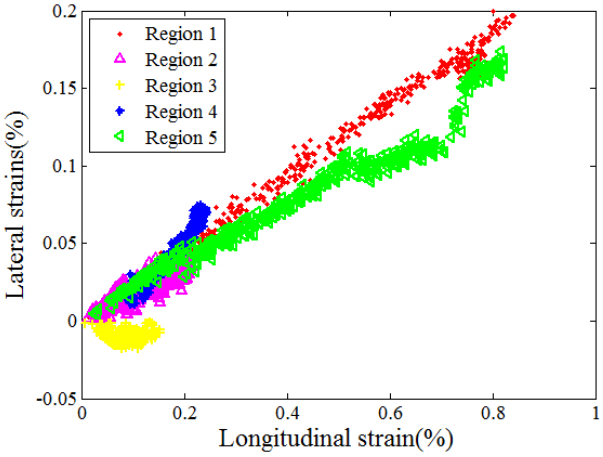

(e) Sample G1-C

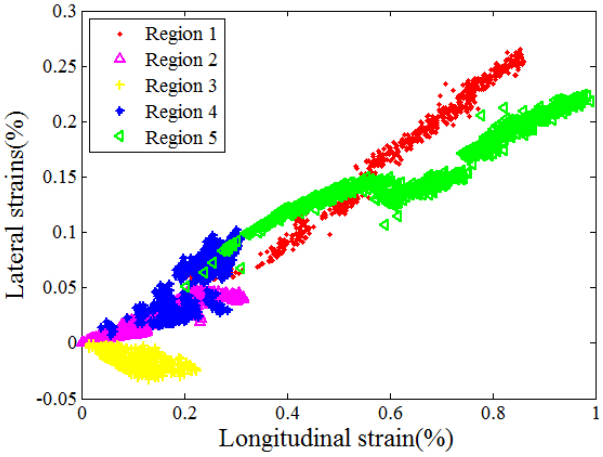

(f) Sample G2-C

Fig.13 Local lateral versus longitudinal strains for the gradient samples of types A, B and C

One striking aspect from the results pertaining the gradient geometry samples is the strong constraining effect on the local distributions of Poisson's ratio by the near-neighboring cells with graded geometry (Fig. 14). Samples G1-A and G2-A should have an intuitive gradient local Poisson's ratio distribution from negative to positive in a progressive manner. Region #5

of the samples G1-A possesses the cell parameters (AR=5 and IS=0.1) that should provide in a uniform perforated metamaterial an in-plane Poisson's ratio of ~ -0.79 (i.e. sample G1-U-1 from Table 6). While region #5 is very close to the artificial tab that provides a strong constraining effect, the local behavior of region #4 shows a constraining effect, with a 51% reduction in magnitude compared to the asymptotic homogenization results [36]. Theoretically the local value of the Poisson's ratio in region #2 should be negative (-0.39 [36]), but in reality is positive. The constraining effect given by the tab in region #1 is also present in this case, although the local Poisson's ratio is rather closer to the asymptotic value (0.375 rather than 0.395 – see also Table 6). A similar trend is also shown by sample G2-A, although with slightly different values because of the different interspace ratio of the cells.

Gradient samples of type B have been initially designed to provide a larger auxetic effect at the centers of the plates, and a more limited transverse deformation towards the ends. Those plates have indeed regions #1 and #5 that possess a positive Poisson's ratio, but those values are limited by the end tabs and the near-neighbor cells (~ 30% compared to asymptotic value [36] and the experimental one of sample G1-U-3). The local Poisson's ratio of region #2 is as expected auxetic, although 25% lower in magnitude compared to the asymptotic result [36]. Regions #4 and #5 are again auxetic and PPR (positive Poisson's ratio), but with lower magnitude values. It is also worth noticing that the distributions of the local Poisson's ratios are not symmetrical about the centers of the plates as theoretically expected. Regions #2 and #3 of the experimental plates show different values of the Poisson's ratios, as well as regions # 4 and 5. Regions #1 are the ones closer to the actuator location, while #5 is where the constraining fixture is present. The two regions show different deformations, with #5 the one with the largest local experimental Poisson's ratios. It is also worth noticing that a certain asymmetry also exists in the FE models, with the local Poisson's ratios of regions #5 higher compared to the ones of regions #1. The different effects provided by the constraints to the nodal degrees of freedom at the base (regions #5) and the uniform displacement applied on the upper tab can be observed in the contour plots of Figure 7.

The gradient configurations C can be considered under a certain extent like mirror images of the configuration B, with the auxetic effect designed to be present at the ends of the plates and the center constrained by a PPR effect. This deformation is clearly present in both in the FEM

and experimental results. It is worth noticing in this case the significantly strong reduction in local experimental Poisson's ratio in the central portion compared to the asymptotic value (0.117 and 0.172 against the 0.39 and 0.44 of the uniform samples – see Table 6). Also, the local negative Poisson's ratios feature some general knock-down factors of 3.2-3.4 compared to the Poisson's ratios provided by the analogous uniform plates. In this case one can also observe an asymmetry of local Poisson's ratios distributions, due to both the experimental compliance and the deformations patters provided by the numerical constraints imposed on the models.

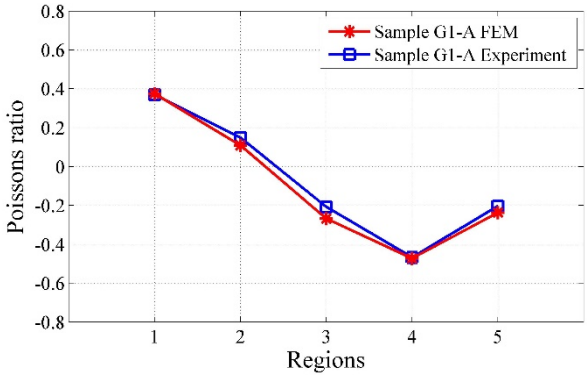

(a) Sample G1-A

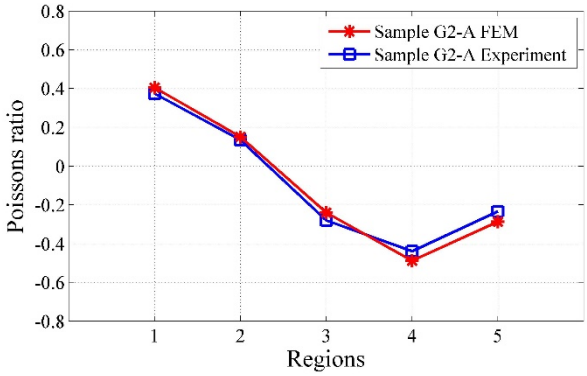

(b) Sample G2-A

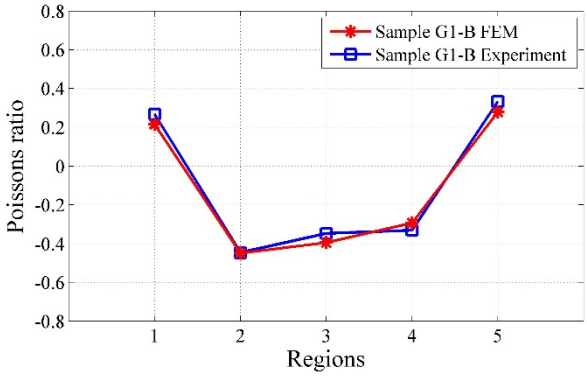

(c) Sample G1-B

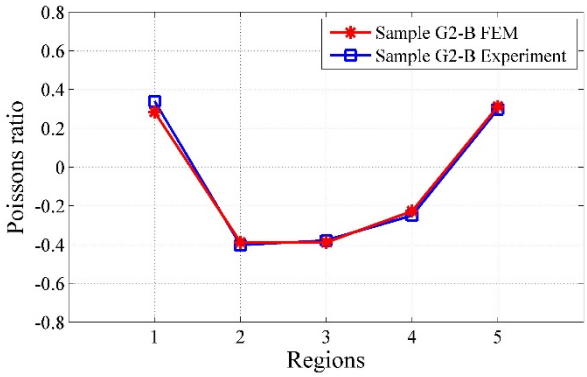

(d) Sample G2-B

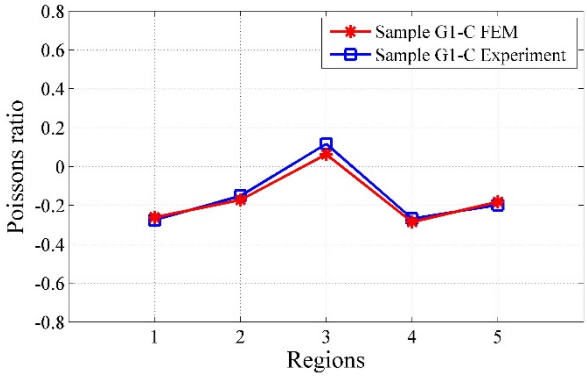

(e) Sample G1-C

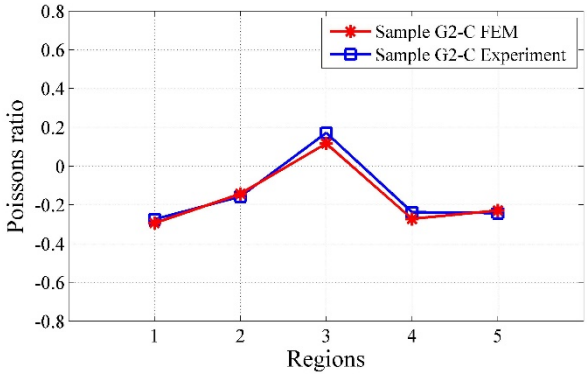

(f) Sample G2-C

Fig.14 Local Poisson's ratio of the regions for the gradient samples of types A, B and C

6 Conclusions

This work has shown the presence of global and local deformation effects due to the application of gradient patterns of centrosymmetric perforations with auxetic behavior. Full-scale samples made out of PMMA material and with patterns produced through laser cutting have been

produced and tested and related finite element models have been developed and benchmarked against results from uniaxial tensile loading. The gradient plates have been designed according to several interspace and aspect ratio values of the cells distributed over five areas distributed symmetrically against the plate centerline. The agreement between the two sets of data is good, and the validated FE models have been able to show very similar patterns of deformations and stress distributions to the experimental datasets.

The use of graded perforated patterns changes significantly the overall behavior of the metamaterial plates. The global stiffness response generally tends to become intermediate between the one provided by cells distributions with the highest and lowest cell interspace values for a given cell aspect ratio, and on average 4% different from the ones related to perforated plates with uniform distributions of cells. The presence of the gradient pattern also generates some local deformation effects provided by the near-neighboring constraints exerted by the surrounding cells with different geometries. These deformations result in local Poisson's ratio values that are smaller in magnitude compared to their asymptotic counterparts. Graded configurations with local central area possessing an asymptotic positive Poisson's ratio behavior show an even greater constraint effect and significant reduction of the local auxetic effect. Scale effects provided by the relative dimensions between the local graded cell areas and the whole dimension of the sample could also play a role, although this aspect is not investigated in this work. The data shown in this paper however suggest that the use of custom graded geometries with perforated slits could provide the metamaterials designer a rich design envelope to create architected materials with highly tailored mechanical behavior at local and non-local scales.

Acknowledgments

This work has been partially supported by the UK EPSRC SYSDYMATS programme. Jianfei Yao would like to thank the Chinese Scholarship Council (CSC) for funding his research work.

References

1. Naebe, M. and K. Shirvanimoghaddam, *Functionally graded materials: A review of fabrication and properties.* Applied Materials Today, 2016. **5**: p. 223-245.

2. Udupa, G., S.S. Rao, and K.V. Gangadharan, *Functionally Graded Composite Materials: An Overview.* Procedia Materials Science, 2014. **5**: p. 1291-1299.
3. Lim, T.C., *Functionally graded beam for attaining Poisson-curving.* Journal of Materials Science Letters, 2002. **21**(24): p. 1899-1901.
4. Lira, C. and F. Scarpa, *Transverse shear stiffness of thickness gradient honeycombs.* Composites Science and Technology, 2010. **70**(6): p. 930-936.
5. Boldrin, L., et al., *Dynamic behaviour of auxetic gradient composite hexagonal honeycombs.* Composite Structures, 2016. **149**: p. 114-124.
6. Lira, C., F. Scarpa, and R. Rajasekaran, *A Gradient Cellular Core for Aeroengine Fan Blades Based on Auxetic Configurations.* Journal of Intelligent Material Systems and Structures, 2011. **22**(9): p. 907-917.
7. Mazloomi, M.S., et al., *Vibroacoustics of 2D gradient auxetic hexagonal honeycomb sandwich panels.* Composite Structures, 2018. **187**: p. 593-603.
8. Shiyin, X., H. Xiuchang, and H. Hongxing, *A study on the isolation performance of trichiral lattices with gradient geometry.* Journal of Vibration and Control, 2014. **21**(16): p. 3465-3475.
9. Ruzzene, M., et al., *Wave Propagation in Sandwich Plates with Periodic Auxetic Core.* Journal of Intelligent Material Systems and Structures, 2002. **13**(9): p. 587-597.
10. Hou, Y., et al., *Graded conventional-auxetic Kirigami sandwich structures: Flatwise compression and edgewise loading.* Composites Part B: Engineering, 2014. **59**: p. 33-42.
11. Imbalzano, G., et al., *A numerical study of auxetic composite panels under blast loadings.* Composite Structures, 2016. **135**: p. 339-352.
12. Imbalzano, G., et al., *Blast resistance of auxetic and honeycomb sandwich panels: Comparisons and parametric designs.* Composite Structures, 2018. **183**: p. 242-261.
13. Bertoldi, K., et al., *Negative Poisson's Ratio Behavior Induced by an Elastic Instability.* Advanced Materials, 2010. **22**(3): p. 361-366.
14. Linforth, S., et al., *Investigation of the auxetic oval structure for energy absorption through quasi-static and dynamic experiments.* International Journal of Impact Engineering, 2021. **147**: p. 103741.
15. Hou, Y., et al., *The bending and failure of sandwich structures with auxetic gradient cellular cores.* Composites Part A: Applied Science and Manufacturing, 2013. **49**: p. 119-131.
16. Ajdari, A., et al., *Mechanical properties of functionally graded 2-D cellular structures: A finite element simulation.* Materials Science and Engineering: A, 2009. **499**(1): p. 434-439.
17. Ajdari, A., H. Nayeb-Hashemi, and A. Vaziri, *Dynamic crushing and energy absorption of regular, irregular and functionally graded cellular structures.* International Journal of Solids and Structures, 2011. **48**(3): p. 506-516.
18. Liu, Y., H.-X. Wu, and B. Wang, *Gradient design of metal hollow sphere (MHS) foams with density gradients.* Composites Part B: Engineering, 2012. **43**(3): p. 1346-1352.
19. Xiao, D. and G. Zhao, *Influence of Gradient Metallic Cellular Core on the Indentation Response of Sandwich Panels.* International Journal of Applied Mechanics, 2017. **09**(03): p. 1750035.
20. Trainiti, G., J.J. Rimoli, and M. Ruzzene, *Optical evaluation of the wave filtering properties of graded undulated lattices.* Journal of Applied Physics, 2018. **123**(9): p. 091706.
21. Evans, K.E. and A. Alderson, *Auxetic Materials: Functional Materials and Structures from Lateral Thinking!*
22. LAKES, R., *Foam Structures with a Negative Poisson's Ratio.* Science, 1987. **235**: p. 1038-1040.
23. Hedayati, R., A.M. Leeflang, and A.A. Zadpoor, *Additively manufactured metallic pentamode meta-materials.* Applied Physics Letters, 2017. **110**(9): p. 091905.
24. Li, H., et al., *Topology optimization for functionally graded cellular composites with metamaterials by*

level sets. Computer Methods in Applied Mechanics and Engineering, 2018. **328**: p. 340-364.
25. Han, Y. and W. Lu, *Evolutionary design of nonuniform cellular structures with optimized Poisson's ratio distribution.* Materials & Design, 2018. **141**: p. 384-394.
26. Wojciechowski, K.W., *Constant thermodynamic tension Monte Carlo studies of elastic properties of a two-dimensional system of hard cyclic hexamers.* Molecular Physics, 1987. **61**(5): p. 1247-1258.
27. Sigmund, O., *Materials with prescribed constitutive parameters: An inverse homogenization problem.* International Journal of Solids and Structures, 1994. **31**(17): p. 2313-2329.
28. N. Grima, J., et al., *On the Auxetic Properties of `Rotating Rectangles' with Different Connectivity.* Journal of the Physical Society of Japan, 2005. **74**(10): p. 2866-2867.
29. Grima, J.N., E. Manicaro, and D. Attard, *Auxetic behaviour from connected different-sized squares and rectangles.* Proceedings of the Royal Society A: Mathematical, Physical and Engineering Sciences, 2011. **467**(2126): p. 439-458.
30. Grima, J.N. and R. Gatt, *Perforated Sheets Exhibiting Negative Poisson's Ratios.* Advanced Engineering Materials, 2010. **12**(6): p. 460-464.
31. N., G.J., et al., *Auxetic Perforated Mechanical Metamaterials with Randomly Oriented Cuts.* Advanced Materials, 2016. **28**(2): p. 385-389.
32. Billon, K., et al., *Numerical tools for efficient simulations of wave propagation in damped periodic structures.* INTER-NOISE and NOISE-CON Congress and Conference Proceedings, 2015. **251**(1): p. 889-896.
33. Shan, S., et al., *Design of planar isotropic negative Poisson's ratio structures.* Extreme Mechanics Letters, 2015. **4**: p. 96-102.
34. Cho, Y., et al., *Engineering the shape and structure of materials by fractal cut.* Proceedings of the National Academy of Sciences, 2014. **111**: p. 17390-17395.
35. Billon, K., et al., *Mechanics and band gaps in hierarchical auxetic rectangular perforated composite metamaterials.* Composite Structures, 2017. **160**: p. 1042-1050.
36. Slann, A., et al., *Cellular plates with auxetic rectangular perforations.* physica status solidi (b), 2015. **252**(7): p. 1533-1539.